Journal of Computational Physics 228 (2009) 1803–1814

Contents lists available at ScienceDirect

Journal of Computational Physics

journal homepage: www.elsevier.com/locate/jcp

Particle-in-Cell modelling of laser–plasma interaction using Fourier decomposition

A.F. Lifschitz [a,b,*], X. Davoine [c], E. Lefebvre [c], J. Faure [b], C. Rechatin [b], V. Malka [b]

[a] Laboratoire de Physique des Gaz et des Plasmas, Université Paris XI/CNRS, Bâtiment 210, 91405 Orsay Cedex, France
[b] Laboratoire d'Optique Appliquée, Ecole Polytechnique/ENSTA/CNRS, 91761 Palaiseau, France
[c] Département de Physique Théorique et Appliquée, CEA/DIF, Bruyères-le-Châtel, 91297 Arpajon Cedex, France

ARTICLE INFO

Article history:
Received 18 April 2008
Received in revised form 23 October 2008
Accepted 10 November 2008
Available online 28 November 2008

Keywords:
Laser–plasma acceleration
Particle-in-Cell simulations
Numerical methods

ABSTRACT

A new Particle-in-Cell code developed for the modelling of laser–plasma interaction is presented. The code solves Maxwell equations using Fourier expansion along the poloidal direction with respect to the laser propagation axis. The goal of the code is to provide a three-dimensional description of the laser–plasma interaction in underdense plasmas with computational load similar to bidimensional calculations. Code results are successfully compared with three-dimensional calculations.

1. Introduction

Experimental and theoretical works performed during the last few years have shown the feasibility of laser–plasma electron acceleration [1–10]. The interaction of a laser pulse with an underdense plasma produces a trail of oscillatory fluctuations of the electron density, e.g. a wakefield. The accelerating gradients in the wakefield can attain extremely high values (of the order of TV/m), exceeding by four orders of magnitude the fields supported in conventional accelerators (some tens of MV/m). Laser–plasma technology is currently considered as very promising in term of development of innovative applications [11]. Laser wakefield acceleration has permitted the production of high quality electron beams of energies up to ≈ 1 GeV [12]. Recently, controlled injection of electrons in the wakefield using a second laser beam has been achieved [13]. Electron beams obtained in this manner are monoenergetic, tuneable and stable.

Numerical modelling of the laser–plasma electron acceleration in the regimes currently explored in the experiments requires a kinetic description of the plasma. Moreover, a number of strongly nonlinear phenomena involved in the interaction are intrinsically three-dimensional, in the sense that they are not well described in 1D or 2D geometries [14]. These phenomena include pulse self-focusing and beam loading. Thus any attempt to bring a realistic description of the process requires the use of a three-dimensional, fully kinetic approach.

The Particle-in-Cell technique is a well established method to solve Vlasov equation for the different plasma species coupled with Maxwell equations. Fully-electromagnetic relativistic Particle-in-Cell codes provide detailed information about the laser–plasma interaction, and they constitute nowadays the most powerful method to study this problem. Several 3D PIC codes have been applied to the study of laser–plasma acceleration, as OSIRIS [15], VLPL [16], CALDER [17] and Vorpal [18]. However, they demand extreme computer resources, and push existing computers to their limits. Indeed, resolving

* Corresponding author. Address: Laboratoire de Physique des Gaz et des Plasmas, Université Paris XI/CNRS, Bâtiment 210, 91405 Orsay Cedex, France.
E-mail address: agustin.lifschitz@u-psud.fr (A.F. Lifschitz).

0021-9991/$ - see front matter © 2008 Elsevier Inc. All rights reserved.
doi:10.1016/j.jcp.2008.11.017

the high frequency laser fields requires to work with small time steps and cell sizes, and therefore, large number of simulations cycles and large grids.

To overcome this difficulty, other codes (WAKE [19], QuickPIC [20]) make use of the ponderomotive force instead of the high frequency laser field. The ponderomotive force varies slowly on the laser frequency (ω_0) timescale, and therefore only the plasma frequency (ω_p) has to be resolved according to this model. The gain in simulation speed is of the order of $(\omega_p/\omega_0)^2$. These codes also use the quasi-static approximation, i.e. assume that the laser pulse does not vary during the time a plasma electron takes to pass the pulse. Within this assumption, only the laser evolution time scale needs to be resolved, even if the cell size must remain smaller than the plasma length (λ_p) (time step and cell size are no longer subject to the Courant condition). These codes are particularly useful for studying very long propagation paths (cm-m) [20,21], for which fully 3D PIC simulations are out of reach. The main drawback of these codes is they cannot describe self-injection or electron trapping in regions of significant laser field. Another limitation comes from the envelope description of the laser, that becomes doubtful when the interaction is strong (large spectral changes, pulse distortion, etc.).

We propose an alternative to fully 3D PIC codes that takes advantage from the symmetry existing in laser–plasma interaction in underdense plasmas. We will show that the use of a Fourier decomposition in a PIC scheme allows us to reduce the computational load to roughly that of a bidimensional simulation while preserving the three-dimensional nature of the interaction, and obtaining a good quantitative agreement with fully 3D simulations.

The structure of this paper is as follows: in Section 2 the mathematical basis of our model are presented. In Section 3 the implementation of the proposed scheme in a numerical code is presented. Results obtained with this code and comparison with 3D PIC simulations are shown in Section 4. Conclusions are presented in Section 5.

2. Mathematical description

We begin by observing that the laser field of a pulse symmetrical under rotation around its propagation axis (x) can be written in cylindrical coordinates as follows:

$$\begin{aligned}\mathbf{E}(\mathbf{r},\mathbf{x},\boldsymbol{\theta},\mathbf{t}) &= E_y(r,x,t)\hat{y} = E_y(r,x,t)(\cos(\theta)\hat{e}_r - \sin(\theta)\hat{e}_\theta)\\ \mathbf{B}(\mathbf{r},\mathbf{x},\boldsymbol{\theta},\mathbf{t}) &= B_z(r,x,t)\hat{z} = B_z(r,x,t)(\sin(\theta)\hat{e}_r + \cos(\theta)\hat{e}_\theta)\end{aligned} \tag{1}$$

with r the radial coordinate $r = \sqrt{y^2+z^2}$. These expressions correspond to a pulse linearly polarized in y ($\theta = 0$, see Fig. 1). The functions $E_y(r,x,t)$ and $B_z(r,x,t)$ can be written as an envelope multiplied by a phase, namely $E_y(r,x,t) = E_0(r,x,t)\sin(k_0x - \omega_0t)$ (in vacuum). We can identify the right-hand-side of Eq. (1) as the first order term ($m = 1$) in a Fourier expansion of the laser field on θ. As Maxwell equations are linear, different Fourier modes evolve independently in vacuum, that is, there is no mode mixing. But modes become coupled when a plasma is present. For example, the laser pulse ($m = 1$ field) will push electrons radially outward producing charge separation and thus creating a $m = 0$ field, i.e. the wakefield. We make the assumption that the main coupling takes place between the zero order mode (the wakefield) and the first order one (the laser field) and that the inclusion of few higher Fourier modes will be enough to describe the laser–plasma interaction process in underdense plasmas. If the first m modes are retained, the calculation load will be roughly equivalent to performing m bidimensional calculations. Note that for a circularly or elliptically polarized pulse, the laser field is also a $m = 1$ field, as can be shown straightforwardly.

We proceed then to decompose the fields in Fourier series,

$$\begin{aligned}\mathbf{F}(r,x,\theta) &= \Re\left(\sum_{m=0}\widehat{\mathbf{F}}^{\mathbf{m}}(r,x)\exp(-im\theta)\right)\\ &= \widehat{\mathbf{F}}^{\mathbf{0}}_{\mathbf{real}}(r,x) + \widehat{\mathbf{F}}^{\mathbf{1}}_{\mathbf{real}}(r,x)\cos(\theta) + \widehat{\mathbf{F}}^{\mathbf{1}}_{\mathbf{imag}}(r,x)\sin(\theta) + \widehat{\mathbf{F}}^{\mathbf{2}}_{\mathbf{real}}(r,x)\cos(2\theta) + \widehat{\mathbf{F}}^{\mathbf{2}}_{\mathbf{imag}}(r,x)\sin(2\theta) + \cdots\end{aligned} \tag{2}$$

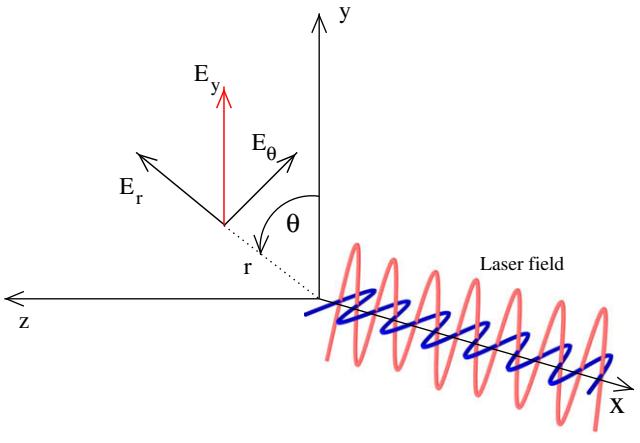

Fig. 1. Definition of axis.

For example, for the linearly polarized field (Eq. (1)), the coefficients in the expansion read

$$\begin{aligned}\widehat{E}^1_r(r,x) &= a(r,x)\\ \widehat{E}^1_\theta(r,x) &= -ia(r,x)\\ \widehat{B}^1_r(r,x) &= ia(r,x)\\ \widehat{B}^1_\theta(r,x) &= a(r,x)\end{aligned} \tag{3}$$

Electric and magnetic fields time evolution is obtained in the PIC code from Faraday's and Ampere's equations,

$$\frac{\partial \mathbf{B}}{\partial t} = -\nabla \times \mathbf{E} \tag{4}$$

$$\frac{\partial \mathbf{E}}{\partial t} = \nabla \times \mathbf{B} - \mathbf{J} \tag{5}$$

Replacing the fields using the expansion given in Eq. (2), we obtain the following set of equations for the coefficients of mode m,

$$\frac{\partial \widehat{B}^m_r}{\partial t} = \frac{im}{r}\widehat{E}^m_x + \frac{\partial \widehat{E}^m_\theta}{\partial x} \tag{6}$$

$$\frac{\partial \widehat{B}^m_\theta}{\partial t} = -\frac{\partial \widehat{E}^m_r}{\partial x} + \frac{\partial \widehat{E}^m_x}{\partial r} \tag{7}$$

$$\frac{\partial \widehat{B}^m_x}{\partial t} = -\frac{1}{r}\frac{\partial}{\partial r}(r\widehat{E}^m_\theta) - \frac{im}{r}\widehat{E}^m_r \tag{8}$$

$$\frac{\partial \widehat{E}^m_r}{\partial t} = -\frac{im}{r}\widehat{B}^m_x - \frac{\partial \widehat{B}^m_\theta}{\partial x} - \widehat{J}^m_r \tag{9}$$

$$\frac{\partial \widehat{E}^m_\theta}{\partial t} = \frac{\partial \widehat{B}^m_r}{\partial x} - \frac{\partial \widehat{B}^m_x}{\partial r} - \widehat{J}^m_\theta \tag{10}$$

$$\frac{\partial \widehat{E}^m_x}{\partial t} = \frac{1}{r}\frac{\partial}{\partial r}(r\widehat{B}^m_\theta) + \frac{im}{r}\widehat{B}^m_r - \widehat{J}^m_x \tag{11}$$

where all the fields and currents are complex functions of (r,x). Currents are calculated by projecting macro-particle velocities over the grid (r,x) and the Fourier modes. The algorithm used is not charge conserving, thus to ensure the fulfillment of the Poisson equation a field E_c is added to the electric field. This correction field is obtained by solving the Poisson equation.

$$\nabla \cdot \mathbf{E_c} = \rho - \nabla \cdot \mathbf{E} \tag{12}$$

Macro-particles advancing is done by the relativistic equation of motion

$$\dot{\mathbf{P}} = q(\mathbf{E} + 1/c\mathbf{v} \times \mathbf{B}) \tag{13}$$

$$\dot{\mathbf{x}} = 1/(m\gamma)\mathbf{P} \tag{14}$$

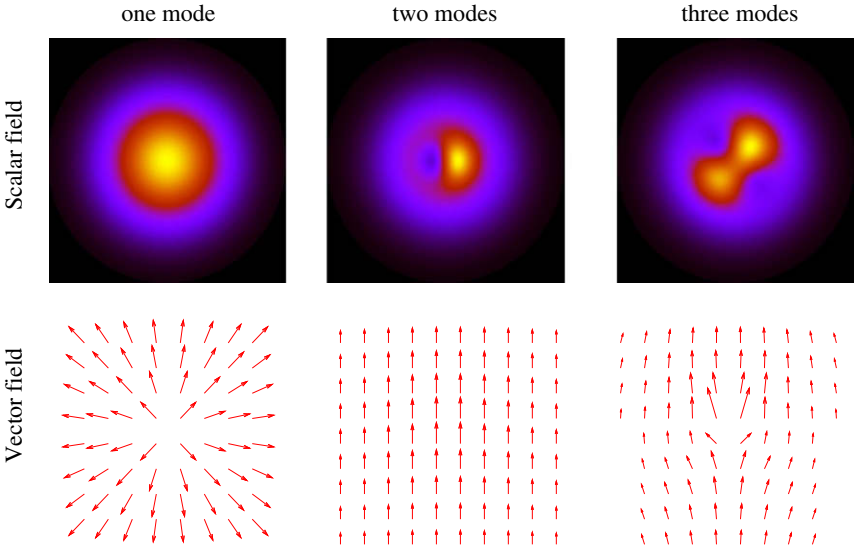

Fig. 2. Examples of scalar (top) and vector (bottom) fields composed of one Fourier mode ($m = 0$), two modes ($m = 0, 1$) and three modes ($m = 0, 1, 2$).

The minimal requirement to simulate the wakefield generation in a plasma is to use the first two Fourier modes, $m = 0$ and $m = 1$. The resulting simulation time is roughly twice the time taken by a bidimensional simulation. The number of modes required to accurately model the interaction will depend on the degree of asymmetry of problem. The origin of the asymmetry can be external (e.g. when trying to model a laser pulse with astigmatism) or intrinsic (e.g. the cross section of a trapped electron bunch can depart from a circular shape). For example, using the first two modes we can describe fields with their maximum off-axis (see Fig. 2), such as the density distribution of an electron bunch trapped off-axis. Using the first three modes ($m = 0, 1, 2$) we can get fields with elliptical shape. This would allow the description of astigmatic laser pulses or electron bunches with elliptical section, as those trapped in the first wake period close to the laser intensity peak.

3. Implementation

Maxwell equations are discretized on the grid with the **E** and **B** fields defined on the Yee lattice [22] (Table 1). Longitudinal and radial cell sizes (Δx and Δr) are uniform all over the grid. Equations are solved in a time-centered scheme, thus allowing consecutive update of the electric and magnetic fields. Macro-particles are advanced using a 2nd-order accuracy scheme. The code offers the option of a moving window.

Macro-particles evolve in the six-dimensional phase space (x, y, z, v_x, v_y, v_z). The current and the charge are projected over the grid with a first-order interpolate scheme as follows: first, we calculate the indexes (i, j) corresponding to the four neighbouring grid points, a straightforward calculation as we use a uniform grid. For example, for the lower left point the indexes are given by

$$\begin{aligned} i &= \lfloor r/\Delta r \rfloor \\ j &= \lfloor x/\Delta x \rfloor \end{aligned} \tag{15}$$

with $r = \sqrt{y^2 + z^2}$. The contribution to the m mode component of the charge density on this point is given by

$$\rho_{ij}^m = C^m \Delta_{ij} q/\Delta V \tag{16}$$

where q is the macroparticle charge, $\Delta_{ij} = ((i+1)^2 - r^2/\Delta r^2)/((i+1)^2 - i^2) \times ((j+1) - x/\Delta x)$ the area-weighting coefficients and ΔV is the cell volume, $\Delta V = 2\pi r \Delta r \Delta x$. Similar expressions can be obtained for the current components. The coefficients C^m can be easily derived using orthogonality of Fourier terms, yielding

$$C^m = e^{im\theta}/\pi \times \begin{cases} 1/2 & \text{if } m = 0 \\ 1 & \text{if } m > 0 \end{cases} \tag{17}$$

Exponentials appearing in this equation can be written as polynomials on y and z. For example, for the first three modes the polynomials are

$$\begin{aligned} C^0 &= 1/(2\pi) \\ C^1 &= (y + iz)/(\pi r) \\ C^2 &= ((y^2 - z^2) + 2iyz)/(\pi r^2) \end{aligned} \tag{18}$$

This kind of direct projection over the modes has the advantage with respect to FFT-based schemes of not requiring an additional 3D mesh to project the sources before performing the transformation. This method is best suited when only a few modes are included in the simulation.

The initial number of particles-per-cell is the same for all the cells. For the uniform density case, the weight of macroparticles is proportional to r.

The code is parallelized via the message passing interface (MPI). Two dimensional domain decomposition is made in the longitudinal and radial directions. Poisson equation is solved using a parallel iterative solver that implements the biconjugate gradient stabilized method.

3.1. Dealing with the axis

The cylindrical coordinate system presents a singularity at $r = 0$ coming from the terms containing the factor $1/r$. The fields E_θ, E_x and B_r are defined in primal grid on r, that includes the axis $r = 0$ (Table 1). Moreover, the fields E_θ and B_r are

Table 1
Grids of definition of fields and sources.

Field	r	x	Source	r	x
E_r	Dual	Primal	J_r	Dual	Primal
E_θ	Primal	Primal	J_θ	Primal	Primal
E_x	Primal	Dual	J_x	Primal	Dual
B_r	Primal	Dual	ρ	Primal	Primal
B_θ	Dual	Dual			
B_x	Dual	Primal			

multivaluated at the axis. Following [23], we will work with these multivaluated fields at $r = 0$ (note than the fields projected over the particles will be always single valuated). The equation for E_θ (Eq. (10)) does not present a singularity. On the other hand, the equations for B_r and E_x (Eqs. (6) and (11), respectively) contain the factor $1/r$, and therefore a method to calculate these fields at the axis is needed.

The electromagnetic fields are not singular at the axis. In general, any scalar or Cartesian field S is single valued, and thus it must fulfill the following condition

$$\left.\frac{\partial S}{\partial \theta}\right|_{r=0} = 0. \tag{19}$$

This implies that for these fields, the $m = 0$ mode is the only one that does not vanish at $r = 0$. This is the case for the fields E_x and B_x, as well as for the scalar fields (as the density). It can be shown that for the cylindrical fields (E_r, E_θ, B_r and B_θ) the $m = 1$ mode is the only one that does not vanish at $r = 0$ [23]. Therefore, we only need to derive equations for the $m = 0$ mode of E_x and for the $m = 1$ mode of B_r.

The value of the $m = 0$ mode longitudinal electric field at the axis can be calculated from the integral form of the Ampere's law. The equation for E_x at the axis semi-discretized in space then reads

$$\frac{\partial(\widehat{E}^0_x)_{0j}}{\partial t} = (\widehat{B}^0_\theta)_{1j}\frac{4}{\Delta r} - (\widehat{J}^0_x)_{0j} \tag{20}$$

We can remove the singularity in Eq. (6) by using the fact that $\widehat{E}^1_z$ vanishes at the axis,

$$\lim_{r\leftarrow 0}\frac{im}{r}\widehat{E}^1_z = im\frac{\partial E^1_z}{\partial r}, \tag{21}$$

thus obtaining the following equation for B_r at the axis:

$$\frac{\partial(\widehat{B}^1_r)_{0j}}{\partial t} = i(\widehat{E}^1_x)_{1j}\frac{1}{\Delta r} + ((\widehat{E}^1_\theta)_{0j} - (\widehat{E}^1_\theta)_{0j-1})\frac{1}{\Delta x} \tag{22}$$

4. Results

4.1. Laser propagation and wakefields

We made a series of simulations to test our assumption, i.e. than only a few Fourier modes are activated by the laser perturbation. We first present simulations corresponding to parameters used in experiments performed with the "*Salle Jaune*" laser at LOA. The laser is linearly polarized in the y direction, with wavelength $\lambda_0 = 0.8\,\mu m$ and peak intensity $I = 3.4 \times 10^{18}$ W cm^{-2}. The pulse has a duration of 30 fs FWHM and it is focused onto a focal spot of 18 μm FWHM. The focal plane is at $x = 0$. The corresponding normalized amplitude of the vector potential is $a_0 = 1.3$ ($a_0 = eA/m_e c^2$, with A the peak value of the laser field vector potential amplitude). Both temporal and radial profiles are Gaussian. The plasma is 2 mm long, with a density $n_e = 7.5 \times 10^{18}$ cm^{-3}. No significant self-injection of plasma electrons into the wakefield is expected for these parameters.

The simulation box size is $68\lambda_0$ in the direction of laser propagation and 188 λ_0 in the transverse direction. Mesh sizes are $\Delta x = \lambda_0/25$ and $\Delta r = \lambda_0/3$. The simulation is performed with 10 macroparticles-per-cell ($N_{ppc} = 10$). That means that in each cell we put 10 particles distributed between $\theta = 0$ and 2π. We made simulations including two Fourier modes ($m = 0 - 1$), three modes ($m = 0 - 2$) and four modes ($m = 0 - 3$). In the three simulations the same number of macroparticles is used. We found that the total plasma density calculated by adding up the contributions of the different modes becomes noisier as the number of modes (M) grows. The noise in the density is due to the use of a number of macroparticles orders of magnitude smaller than number of physical particles (sampling noise). The signal-to-noise ratio for a given mode m follows the same scaling law as in Cartesian PIC schemes, that is,

$$\mathrm{SNR}^m = \left(\sum_{i,j}(\bar{\rho}^m_{ij})^2 \Big/ \sum_{i,j}(\rho^m_{i,j} - \bar{\rho}^m_{ij})^2\right)^{1/2} \propto N^{1/2}_{ppc} \tag{23}$$

with the indexes i and j running, respectively, in $[1, N_r]$ and $[1, N_x]$. For the total density calculated including the contributions of M modes, the signal-to-noise ratio follows the scaling $\mathrm{SNR} \propto (N_{ppc}/M)^{1/2}$, i.e. the effective number of particles-per-cell is divided by M. To keep the same noise level when adding Fourier modes requires to multiply N_{ppc} by $\sqrt{M}$.

The maximum normalized transverse field E_y as the laser propagates in the plasma obtained in these three cases is shown in Fig. 3 (with $E_0 = \omega_0 m_e c/e$). All the electric fields in this section are in units of E_0. The laser pulse propagates from the left ($x = 0$) to the right. The pulse is strongly self-focused, reaching a maximum amplitude of $a_0 \approx 3$ at $x = 860\,\mu m$. Then the pulse diffracts, and it presents a second self-focusing phase from $x = 1300\,\mu m$. As expected, self-injection does not occur in the simulation. We can see that the curves obtained for the laser amplitude are very close for the three cases. This indicates that the laser pulse propagation does not change when adding Fourier modes with $m > 1$.

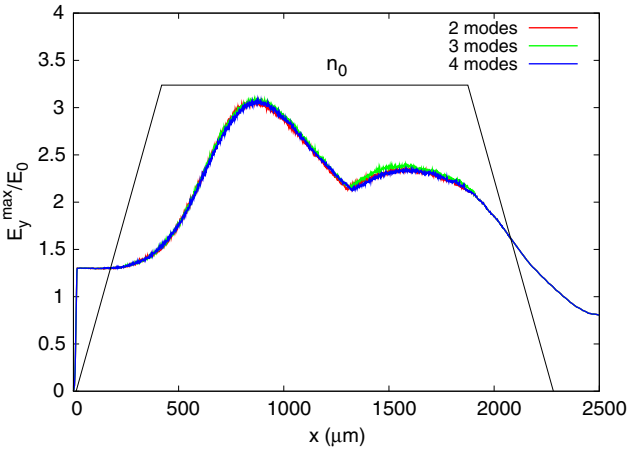

Fig. 3. Maximum transverse electric field E_y^{max} vs. x for $a_0 = 1.3$ and $w_0 = 18$ μm obtained including the modes $m = 0-1, m = 0-2$ and $m = 0-3$. Plasma density profile is also shown.

The same trend is found at higher laser intensities. The evolution of the laser amplitude for $a_0 = 5$ and focal spot of 9 μm FWHM is shown in Fig. 4. To reduce the numerical noise, we use 20 ppc, twice more than in the previous simulations. The other parameters remain unchanged. Self-focusing produces a peak around $x = 280$ μm, with $a_0 = 7.4$. Around $x = 350$ μm self-injection of electrons in the first wake period starts. From $x = 500$ μm the laser pulse propagates as in a self-channeled mode and does not undergo large amplitude oscillations. As in the lower intensity case, the evolution of the laser amplitude does not change when including more Fourier modes in the simulation. Simulations made for a large range of parameters confirm the fact that the evolution of the laser pulse does not change significantly if higher modes are included in the simulation.

Inspection of the longitudinal profile of the transverse field allows us to get more information about the importance of different orders in the Fourier expansion. We can see in Fig. 5 a screenshot of the transverse field as a function of x ($y = 1$ μm,$z = 0$) when the laser pulse is at $x \approx 285$ μm. The contributions of each of the three modes included in the simulation are shown separately. Note that the fields that we expand in Fourier series are E_r and E_θ and not E_y and E_z. With the contribution of the mode m to E_y we refer to the E_y field calculated from the contributions of the mode m to E_r and E_θ,

$$E_y^m = E_r^m(\theta)\cos(\theta) - E_\theta^m(\theta)\sin(\theta) \tag{24}$$

Fields are plotted off-axis because for symmetry reasons the contribution of even modes to E_y are null at the axis. As expected, a low frequency contribution of the mode $m = 0$ appears, and this contribution is small compared with the input laser field $m = 1$. This field with poloidal symmetry ($m = 0$) is the radial field of the wakefield. It presents two peaks around $x \approx 273$ μm and $x \approx 255$ μm, corresponding to the back of the first and second wake periods, respectively. This large localised radial field is associated with a large electron density peak occurring at the back of each wake period in the strongly nonlinear interaction regime. On the other hand, the contribution of the $m = 2$ mode is negligible compared with the lower order modes.

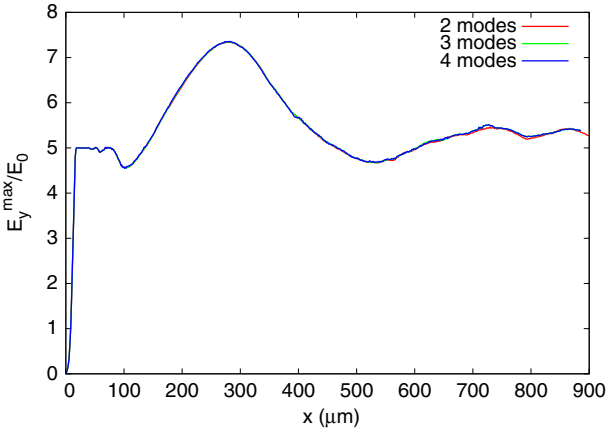

Fig. 4. Maximum transverse electric field E_y^{max} vs. x for $a_0 = 5$ and $w_0 = 9$ μm obtained including the modes $m = 0-1, m = 0-2$ and $m = 0-3$.

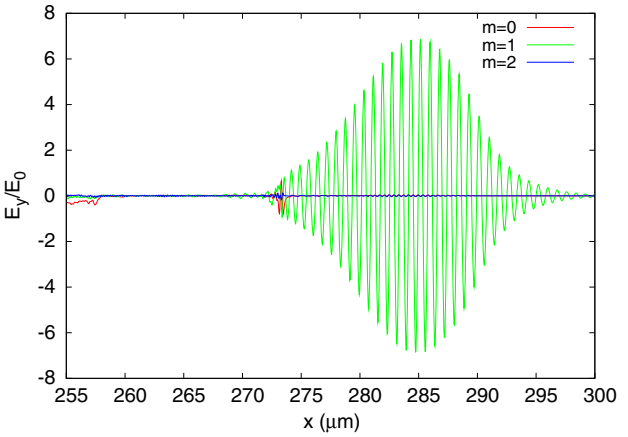

Fig. 5. Contribution of different modes to the transverse electric field E_y/E_0 at $(y,z) = (1,0)$ μm for $a_0 = 5$ and $w_0 = 9$ μm.

The longitudinal field E_x presents a marked dependency with the poloidal angle θ. In the $x-z$ plane (perpendicular to the laser polarization vector, Fig. 6(a)) only the $m = 0$ mode takes significant values. This low frequency field corresponds to the wake longitudinal field. On the other hand, in the $x-y$ plane (parallel to the laser polarization vector) the longitudinal field presents a significant contribution from the $m = 0$ and $m = 1$ modes. As shown in Fig. 6(b), inside the pulse there is a significant contribution of the $m = 1$ mode that varies on the scale of the laser wavelength. This field arises from the finite radial extension of the laser pulse, as can be seen by inserting in Eq. (11) the magnetic field given by Eq. (3) and neglecting J_x^1, thus obtaining

$$\frac{\partial \widehat{E}_x^1}{\partial t} = \frac{\partial a(r,x)}{\partial r} \Rightarrow \frac{\partial E_x^1}{\partial t} = \frac{\partial E_0(x,r)}{\partial r} \sin(k_0 x - \omega_0 t)\cos(\theta) \tag{25}$$

In the $x-y$ plane ($\theta = 0$) the high frequency longitudinal field takes its maximum value, whereas it vanishes in the $x-z$ plane ($\theta = \pi/2$). In both cases, the contribution of the $m = 2$ mode is negligible.

The total longitudinal field that results from the superposition of all modes is shown in Fig. 7. In the $x-z$ plane we retrieve the low frequency wakefield, whereas in the $x-y$ plane the high frequency component coming from the $m = 1$ mode is present. We can see that this field can be as large as the wakefield for cases of tight focusing as presented here (the spot diameter is $\simeq 10.6$ μm FWHM for this case). It can constitute a deleterious effect over the quality of bunches accelerated in the the first wake as it introduces a large oscillation of the accelerating field at the λ_0 scale, thus reducing the monochromaticity of the extracted bunch. This effect can be overcome by using shorter pulses or loose focusing.

The spatial distribution of electron density at $x = 850$ μm (500 μm after the onset of self-injection, that arises around $x \simeq 350$ μm) is shown in Fig. 8. The first two wake periods are shown in this plot. An electron bunch is trapped in the first wake period or "bubble", and a second bunch is trapped in the second wake period. The electron energy spectrum presents a peak around 180 MeV (Fig. 9), that corresponds to the bunch trapped in the first wake. The charge in this peak is 350 pC. The effective accelerating field obtained for these parameters is close to 360 MeV/mm.

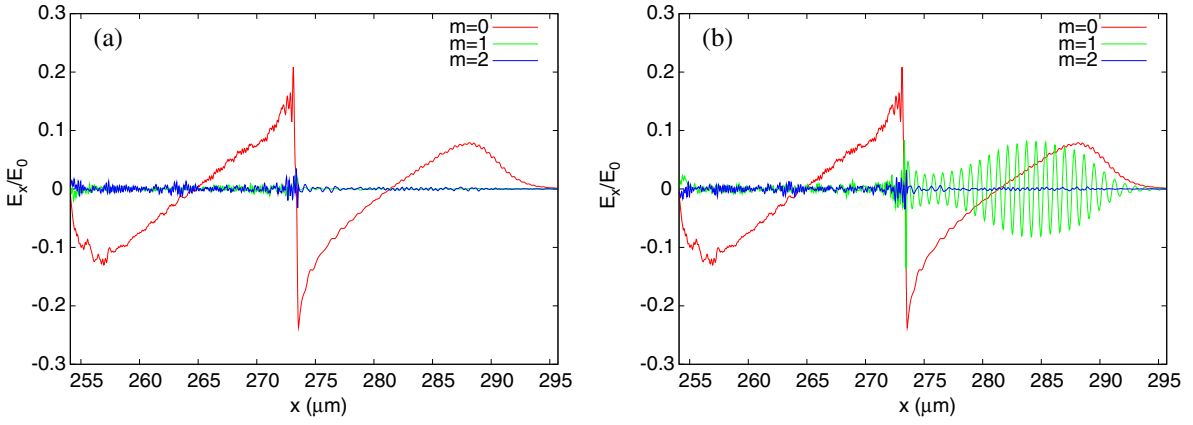

Fig. 6. Contribution of different modes to the longitudinal electric field E_x vs. x at $(y,z) = (1,0)$ μm (a) and $(y,z) = (0,1)$ μm (b) for $a_0 = 5$ and $w_0 = 9$ μm.

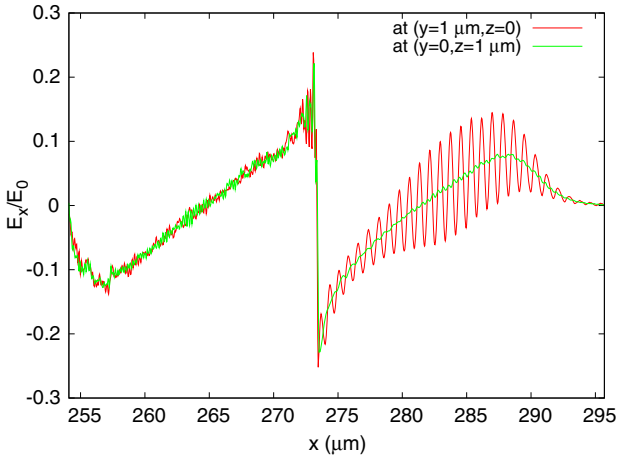

Fig. 7. Longitudinal electric field E_x vs. x at $(y,z) = (1,0)$ μm and $(y,z) = (0,1)$ μm for $a_0 = 5$ and $w_0 = 9$ μm.

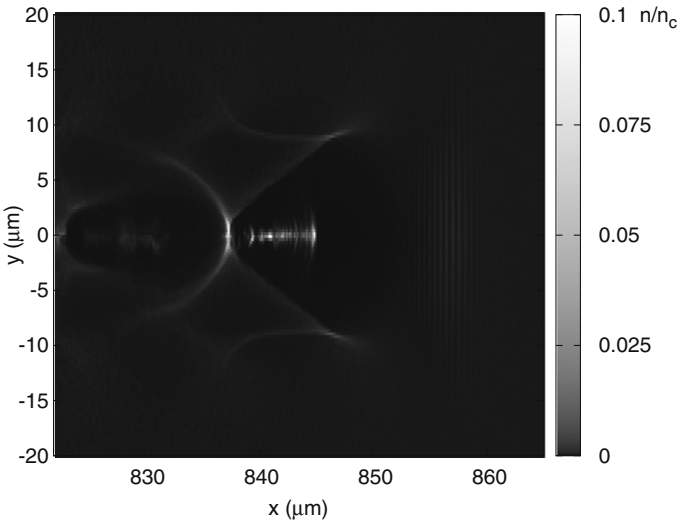

Fig. 8. Spatial distribution of electron density in the plane $x - y$ at $x = 850$ μm.

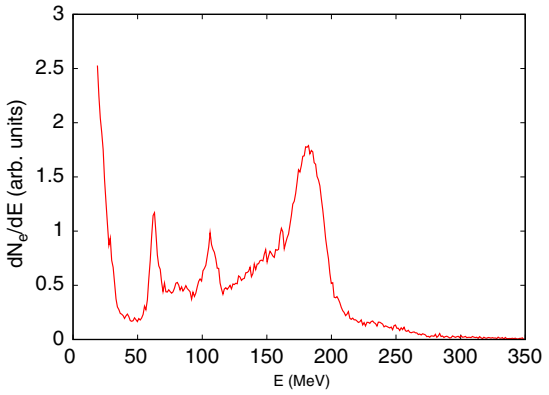

Fig. 9. Electron energy spectrum at $x = 850$ μm. Charge in the peak is 350 pC.

The spatial distribution of longitudinal electric field in the $x-y$ and $x-z$ planes are shown in Fig. 10. In the $x-z$ plane (10.b) the field is smooth on the λ_p scale, whereas in the plane of laser polarization $x-y$ (10.a) there is the high frequency contribution coming from the mode $m=1$ discussed above.

The inclusion of higher order modes ($m>2$) becomes necessary when dealing with large laser intensities. As mentioned above, electron bunches trapped in the first wake period are larger in the direction of laser polarization (y) than in perpendicular direction (z) [24]. The inclusion of the $m=2$ mode is needed to deal with this kind of asymmetry (see Fig. 2). But at high intensity, the deformation can be large [25] and more modes are needed to model it.

4.2. Comparison with 3D simulations

We present in this section a comparison between the results obtained with our new code and three-dimensional simulations performed with the fully-electromagnetic PIC code CALDER [17]. Simulation parameters have been chosen to reduce as much as possible the size of the simulation box in the 3D simulations. We raise the value of density to $n_e = 1.2\times10^{19}$ cm^{-3}, to get a stronger self-focusing and a narrower beam. The pulse with amplitude $a_0=5$ and $\tau=30$ fs has a focal spot of 9 μm FWHM. Three-dimensional simulations are performed with 4 ppc and a third-order interpolation scheme, whereas Fourier simulations are done with 20 ppc, a first-order interpolation scheme, and three Fourier modes. Three-dimensional simulations are performed using a time step $\Delta t = 0.24\omega_0^{-1}$ with a mesh of $1600\times160\times160$ cells of size $\Delta x = 0.25k_0^{-1}, \Delta y=\Delta z=2.5k_0^{-1}$, corresponding to 160×10^6 macroparticles. In the Fourier simulations the time step is $\Delta t=0.24\omega_0^{-1}$ with a mesh of 1600×200 cells of size $\Delta x=0.25k_0^{-1}$ and $\Delta r=1k_0^{-1}$ and 6×10^6 macroparticles. The three-dimensional runs took roughly 7000 CPU hours (17 h in 400 processors). Fourier simulations took 70 CPU hours (12 h in six processors), 100 times less than the 3D ones.

Two cases are considered. In the first one, the plasma presents a parabolic density profile in the radial direction, that improves the guiding thus reducing the amount of laser energy reaching the transverse boundaries of the simulation box. In the second case, the plasma is homogeneous.

The evolutions of the laser amplitude for the parabolic density profile plasma and for the uniform plasma are shown in Fig. 11. In both cases the evolution is rather complex, with several cycles of self-focusing/divergence. In the case of the parabolic profile (Fig. 11(a)), the agreement is very good between both codes. From $x=800$ μm, the 3D curve presents rapid oscillations, that are related with the arising of a peak in the laser longitudinal profile with length of the order of λ_0. For the uniform plasma (Fig. 11(b)), there is a small difference from $x=600$ μm. We consistently found an overestimation of the laser amplitude in the 3D simulations with respect to that obtained with the present code, when the transverse section of the simulation box is so small as to allow a significant laser field to reach the boundary (periodic conditions are used in the transverse boundaries in the 3D calculation). In the case of the parabolic plasma, the laser pulse is best guided and it can be expected that this effect would be less important. The shapes of the laser pulses obtained with the Fourier and the 3D codes are also in good agreement (Fig. 12).

The longitudinal electric field for the uniform plasma case is shown in Fig. 13. The results obtained with the Fourier and the 3D codes are again very close. In the $x-y$ plane we can see the high frequency field superimposed to the wakefield in the first wake period, which is associated with the finite laser pulse radius as already mentioned. As expected, this field is absent in the $x-z$ plane in both simulations.

The spatial distribution of electron density for the uniform plasma is shown in Fig. 14. In this screenshot, corresponding to $x=640$ μm, we can see that there is an electron bunch trapped in the first wake period. The density distribution of the bunch

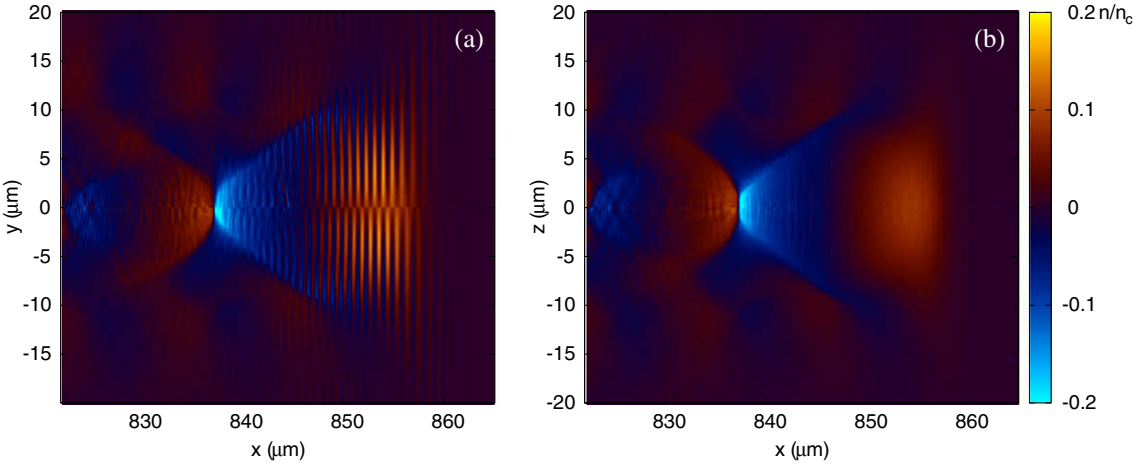

Fig. 10. Spatial distribution of longitudinal electric field in the $x-y$ (a) and $x-z$ (b) planes.

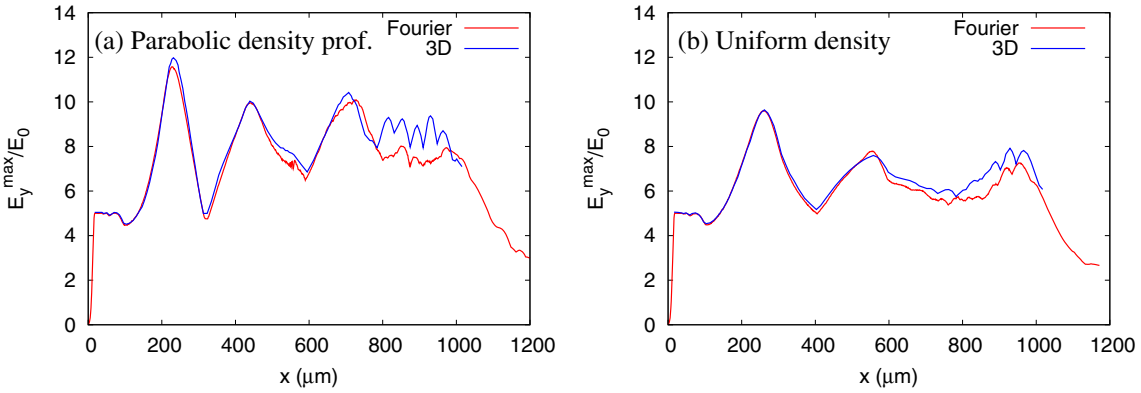

Fig. 11. Maximum transverse electric field E_y vs. x for a parabolic radial density profile (a) and a uniform density profile (b). Fourier and 3D results are shown.

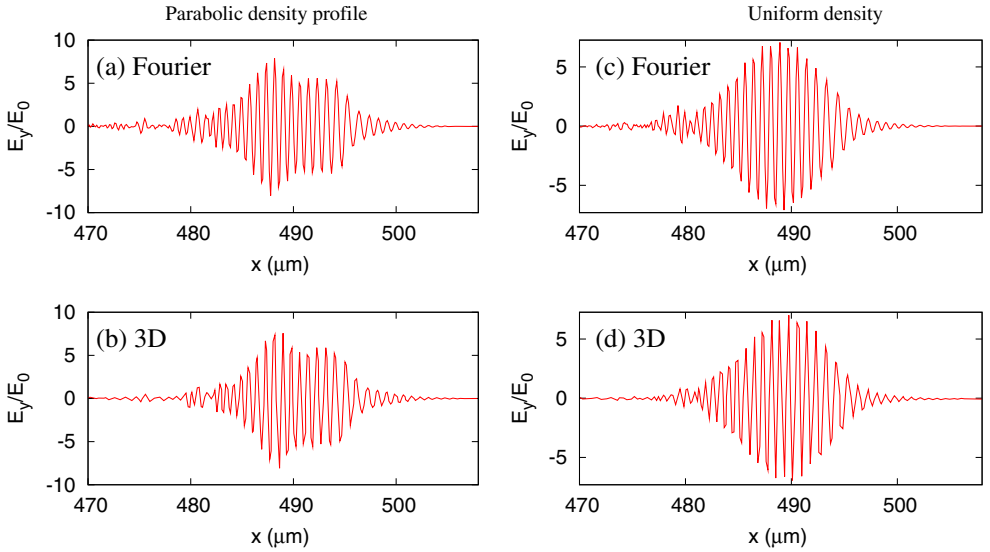

Fig. 12. Transverse electric field E_y at the axis vs. x for a parabolic radial density profile (left) and a uniform density profile (right). The results obtained with our new code (top) and 3D simulations (bottom) are shown.

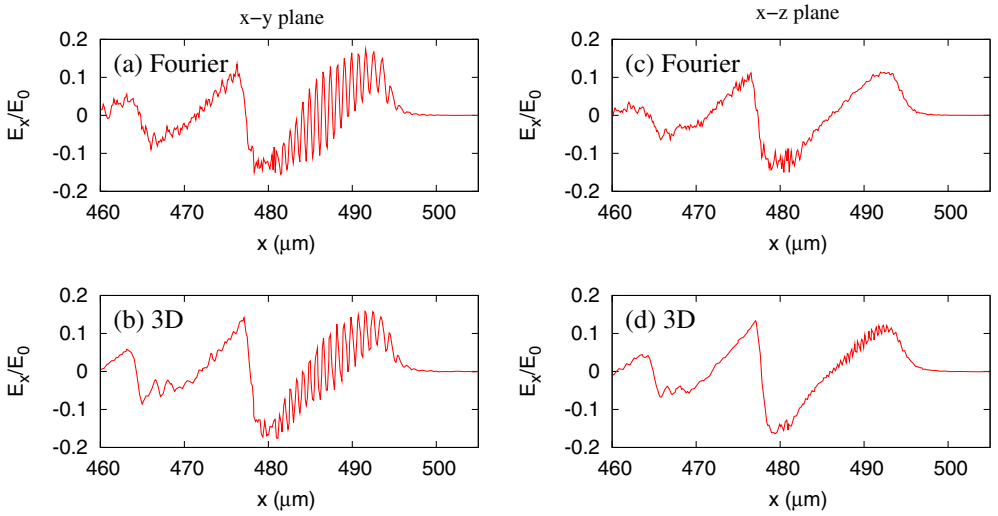

Fig. 13. Longitudinal electric field E_x vs. x for a uniform density case at $(y,z) = (1,0)$ μm (left) and $(y,z) = (0,1)$ μm (left). The results obtained with the present code (top) and 3D simulations (bottom) are shown.

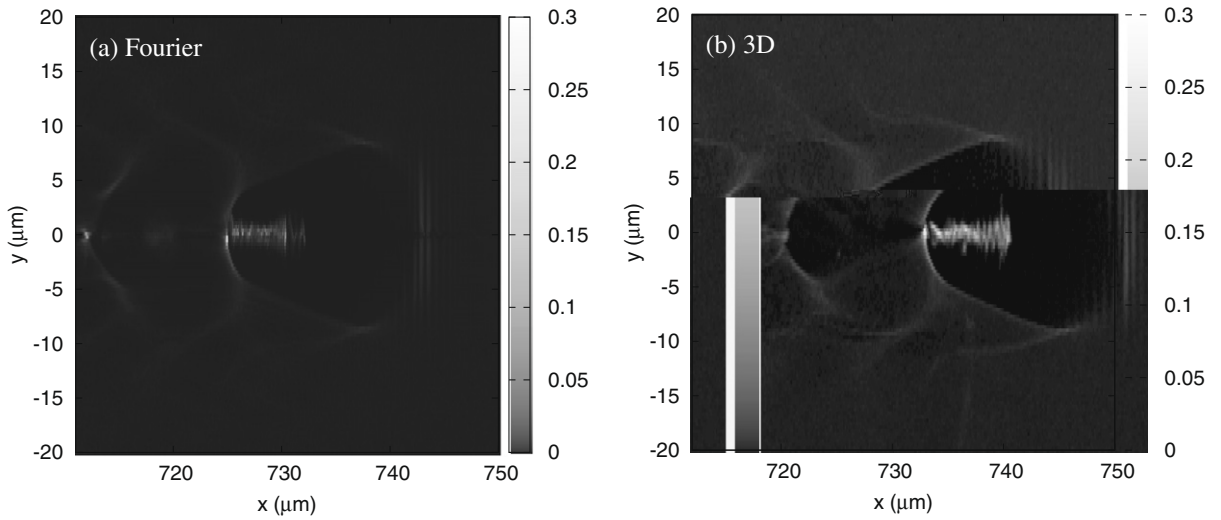

Fig. 14. Spatial distribution of electron density at $x = 740$ μm for the uniform density case in the plane $x - y$ ($z = 0$).

is similar in the Fourier and 3D simulations, even if in the 3D simulation the radial spread at the head of the bunch and the pulse length are somewhat larger than in the Fourier simulation.

5. Conclusions

In this paper, we have presented a relativistic Particle-in-Cell code based on a Fourier decomposition of the electromagnetic fields developed to study laser–plasma interaction in underdense plasmas. The code allows a kinetic description of the problem preserving the three-dimensional nature of the system with computer loads comparable to bidimensional calculations. Results of the code are in good agreement with those of fully 3D simulations.

Acknowledgments

The authors acknowledge the support of the European Community Research Infrastructure Activity under the FP6 "Structuring the European Research Area" program (CARE, Contract No. RII3-CT-2003-506395). Allocation of computer resources by the Informatic Direction (DI, Université Paris Sud) is also gratefully acknowledged.

References

[1] A. Modena, Z. Najmudin, A.E. Dangor, C.E. Clayton, K.A. Marsh, C. Joshi, V. Malka, C.B. Darrow, D. Neely, F.N. Walsh, Electron acceleration from the breaking of relativistic plasma waves, Nature 337 (1995) 606.
[2] V. Malka et al., Electron acceleration by a wake field forced by an intense ultrashort laser pulse, Science 298 (2002) 1596–1600.
[3] D. Umstadter, S.Y. Chen, A. Maksimchuk, G. Mourou, R. Wagner, Nonlinear optics in relativistic plasmas and laser wake field, Science 273 (1996) 472.
[4] C. Gahn, G.D. Tsakiris, A. Pukhov, J. Meyer-ter-Vehn, G. Pretzler, P. Thirolf, D. Habs, K.J. Witte, Multi-MeV electron beam generation by direct laser acceleration in high-density plasma channels, Phys. Rev. Lett. 83 (1999) 4772.
[5] Y. Kitagawa et al., Beat-wave excitation of plasma wave and observation of accelerated electrons, Phys. Rev. Lett. 68 (1992) 48.
[6] F. Amiranoff et al., Observation of laser wakefield acceleration of electrons, Phys. Rev. Lett. 81 (1998) 995.
[7] M. Everett, A. Lal, D. Gordon, C.E. Clayton, K.A. Marsh, C. Joshi, Trapped electron acceleration by a laser-driven relativistic plasma wave, Nature 368 (1994) 527.
[8] S.P.D. Mangles et al., Monoenergetic beams of relativistic electrons from intense laser–plasma interactions, Nature 431 (2004) 535–538.
[9] C.G.R. Geddes, Cs. Toth, J. van Tilborg, E. Esarey, C.B. Schroeder, D. Bruhwiler, C. Nieter, J. Cary, W.P. Leemans, High-quality electron beams from a laser wakefield accelerator using plasma-channel guiding, Nature 431 (2004) 538–541.
[10] J. Faure, Y. Glinec, A. Pukhov, S. Kiselev, S. Gordienko, E. Lefebvre, J.-P. Rousseau, F. Burgy, V. Malka, A laser–plasma accelerator producing monoenergetic electron beams, Nature 431 (2004) 541–544.
[11] V. Malka, J. Faure, Y.A. Gauduel, E. Lefebvre, A. Rousse, K.T. Phuoc, Principles and applications of compact laser-plasma accelerators, Nature Phys. 4 (2008) 447–453.
[12] W.P. Leemans et al., GeV electron beams from a centimetre-scale accelerator, Nature Phys. 2 (2006) 696–699.
[13] J. Faure, C. Rechatin, A. Norlin, A. Lifschitz, Y. Glinec, V. Malka, Controlled injection and acceleration of electrons in plasma wakefields by colliding laser pulses, Nature 444 (2006) 737.
[14] X. Davoine, E. Lefebvre, J. Faure, C. Rechatin, A. Lifschitz, V. Malka, Simulation of quasi-monoenergetic electron beams produced by colliding pulse wakefield acceleration, Phys. Plasmas 15 (2008) 113102.
[15] R.A. Fonseca et al., OSIRIS: a three-dimensional, fully relativistic particle in cell code for modeling plasma based accelerators, in: P.M.A. Sloot et al. (Ed.), ICCS 2002, LNCS, vol. 2331, 2002, pp. 342–351.
[16] A. Puhkov, 3D electromagnetic relativistic Particle-In-Cell code VLPL(virtual laser plasma lab), J. Plasma Phys. 61 (1999) 425–433.
[17] E. Lefebvre et al., Electron and photon production from relativistic laserplasma interactions, Nucl. Fusion 43 (2003) 629–633.
[18] C. Nieter, J.R. Cary, VORPAL as a tool for the study of laser pulse propagation in LWFA, Lect. Notes Comput. Sci. 2331 (2002) 334–341.

[19] P. Mora, T.M. Antonsen, Electron cavitation and acceleration in the wake of an ultra-intense, self focused laser pulse, Phys. Rev. E 53 (1996) 2068.
[20] C. Huang et al., QuickPIC: a highly efficient fully parallelized PIC code for plasma-based acceleration, J. Phys: Conf. Ser. 46 (2006) 190–199.
[21] A.F. Lifschitz, J. Faure, Y. Glinec, V. Malka, P. Mora, Proposed scheme for compact GeV laser plasma accelerator, Las. Part. Beams 24 (2006) 255–259.
[22] K.S. Yee, Numerical solution of initial boundary value problems involving Maxwell's equations in isotropic media, IEEE Trans. Antennas Propag. AP-14 (1966) 302–307.
[23] S.G. Constantinescu, S.K. Lele, A highly accurate technique for the treatment of flow equations at the polar axis in cylindrical coordinates using series expansions (2002), J. Computat. Phys. 183 (2002) 165.
[24] S.P.D. Mangles et al., Laser-wakefield acceleration of monoenergetic electron beams in the first plasma-wave period, Phys. Rev. Lett. 96 (2006) 215001.
[25] M. Kando et al., On the production of flat electron bunches for laser wakefield acceleration, J. Exp. Th. Phys. 105 (2007) 916–926.